Thermal fluctuations of grafted microtubules provide evidence of a length-dependent persistence length

Francesco Pampaloni*†, Gianluca Lattanzi†‡, Alexandr Jonáš§, Thomas Surrey*, Erwin Frey¶‖, and Ernst-Ludwig Florin§‖

*Cell Biology and Biophysics Unit, European Molecular Biology Laboratory, Meyerhofstrasse 1, D-69117 Heidelberg, Germany; ‡Department of Medical Biochemistry, Biology, and Physics, Innovative Technologies for Signal Detection and Processing Center and Instituto Nazionale Fisica Nucleare, Università di Bari, Piazza Giulio Cesare 11, 70124 Bari, Italy; §Center for Nonlinear Dynamics, University of Texas, Austin, TX 78712; and ¶Arnold Sommerfeld Center for Theoretical Physics and Center for Nano Science, Department of Physics, Ludwig-Maximilians-Universität München, Theresienstrasse 37, D-80333 Munich, Germany

Communicated by Robert H. Austin, Princeton University, Princeton, NJ, May 13, 2006 (received for review June 25, 2005)

Microtubules are hollow cylindrical structures that constitute one of the three major classes of cytoskeletal filaments. On the mesoscopic length scale of a cell, their material properties are characterized by a single stiffness parameter, the persistence length ℓ_p. Its value, in general, depends on the microscopic interactions between the constituent tubulin dimers and the architecture of the microtubule. Here, we use single-particle tracking methods combined with a fluctuation analysis to systematically study the dependence of ℓ_p on the total filament length L. Microtubules are grafted to a substrate with one end free to fluctuate in three dimensions. A fluorescent bead is attached proximally to the free tip and is used to record the thermal fluctuations of the microtubule's end. The position distribution functions obtained with this assay allow the precise measurement of ℓ_p for microtubules of different contour length L. Upon varying L between 2.6 and 47.5 μm, we find a systematic increase of ℓ_p from 110 to 5,035 μm. At the same time we verify that, for a given filament length, the persistence length is constant over the filament within the experimental accuracy. We interpret this length dependence as a consequence of a nonnegligible shear deflection determined by subnanometer relative displacement of adjacent protofilaments. Our results may shine new light on the function of microtubules as sophisticated nanometer-sized molecular machines and give a unified explanation of seemingly uncorrelated spreading of microtubules' stiffness previously reported in literature.

nanomechanics | protofilaments | single-particle tracking | thermal fluctuation analysis

The mechanics of living cells is largely determined by the cytoskeleton, a self-organizing and highly dynamic network of filamentous proteins of different lengths and stiffnesses (1). Understanding the elastic response of purified cytoskeletal filaments is fundamental for the elucidation of the rheological behavior of the cytoskeleton. Microtubules (MTs) are hollow cylindrical filaments formed by, on average, 13 tubulin protofilaments (PFs) assembled in parallel. The MT outer and inner diameters are ≈25 and 15 nm, respectively. In cells, MTs are generally 1–10 μm long, whereas in axons their length can be 50–100 μm (2).

The tubular structure of MTs implies a minimal cross-sectional area, hence a high strength and stiffness combined with low density. In recent years, the mechanical properties of MTs have been investigated by several experimental approaches, such as thermal fluctuations (3–6), atomic force microscopy (AFM) (7–10), and optical tweezers (11–13).

The standard reference model to describe the mechanical properties of a biopolymer on length scales much larger than any microscopic scale (the tube diameter for MTs) is the worm-like chain model (14, 15). It is characterized in terms of a flexural rigidity κ (neglecting torsional rigidity). The combined effect of flexural rigidity and thermal fluctuations on the conformation of the filament is given by the ratio κ/k_BT, which defines a characteristic length scale, the persistence length ℓ_p. In a fluctuation analysis, ℓ_p determines the width of the probability distribution functions of the filament contour, e.g., the probability distribution function of the end-to-end distance of the filament $P(R)$ (16). The relationship between the flexural rigidity, or equivalently ℓ_p, with the architecture of the MT and the molecular interactions between the constituent dimeric tubulin proteins is, in general, non trivial. Trivial relationships will hold only in the case of simple architectures. For example, in the case of a homogeneous elastic rod with a fixed cross section and a Young modulus E, $\kappa = EI$, where I is the second moment of area of the cross section.

Recently, there has been clear experimental evidence that a model that relates κ to a single modulus E is too naive: for taxol-stabilized MTs the measured flexural rigidities vary in a large range between 1.9×10^{-24} nm^2 (11) and 2.15×10^{-23} nm^2 (3). The rigidity values of not-stabilized MTs range between 4.7×10^{-24} nm^2 (11) and 3.4×10^{-23} nm^2 (4). The origin of this scattering is still a matter of debate. Recently, it was shown that increasing the growth velocity *in vitro* may decrease the MT rigidity by a factor of 2 (4). However, this is not sufficient to explain the observed broad range of MT stiffness values reported in literature.

We suggest that the solution of this puzzle might be looked for rather in the complex mechanical behavior due to strongly anisotropic material properties of MTs. Although usually modeled as isotropic cylinders in literature, MTs have strongly anisotropic elastic properties determined by their discrete PF structure: inter-PF bonds are weaker than the head–tail $\alpha\beta$–$\alpha\beta$ tubulin bonds along the PF (7, 8, 17, 18), and adjacent PFs can slightly shift relatively to each other (19). Hence, it is expected that, in the language of continuum mechanics, the shear modulus G of a MT (determined by the deformability of lateral bonds) differs significantly from its Young's modulus E (9, 10, 20) (determined by longitudinal tubulin interactions along the PFs). Indeed, recent experiments with AFM yielded a shear modulus that was 2–3 orders of magnitude smaller than the Young's modulus (9, 10, 20). Moreover, an extremely low transverse buckling stress of $P_r = 600$ Pa has been measured on MTs (21) subject to osmotic pressure. This is four orders of magnitude smaller than the buckling stress calculated by modeling a MT as an isotropic shell with $E \sim 1.6$ GPa.

From engineering literature on fiber reinforced materials, it is known that a key parameter is the total filament length L. The main goal of this work is a systematic study of the dependence of ℓ_p on L, by performing a thermal fluctuation analysis that exploits the fact that the random fluctuations of the polymer

Conflict of interest statement: No conflicts declared.

Abbreviations: AFM, atomic force microscopy; MT, microtubule; PF, protofilament.

†F.P. and G.L. contributed equally to this work.

‖To whom correspondence may be addressed. E-mail: frey@lmu.de or florin@chaos.utexas.edu.

www.pnas.org/cgi/doi/10.1073/pnas.0603931103

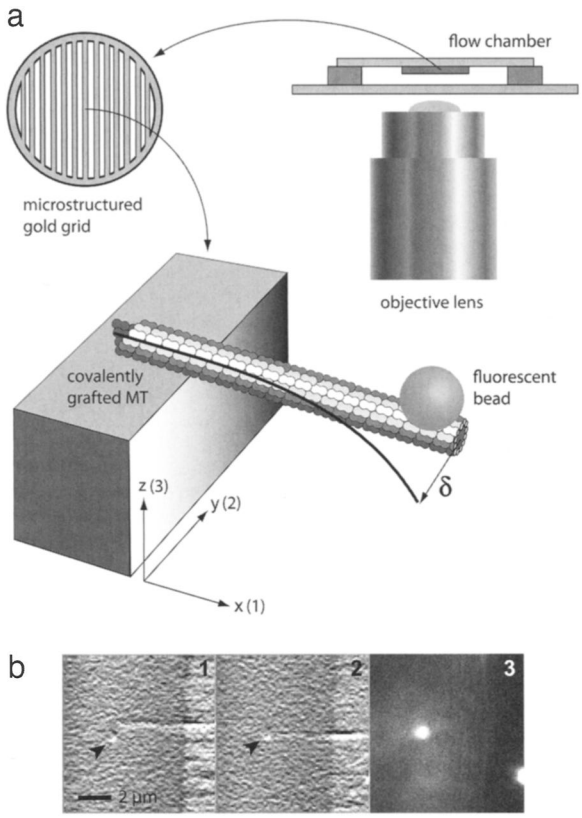

Fig. 1. Representation of the experimental situation. (*a*) The MT is covalently grafted on a gold substrate. A fluorescent colloidal bead (not to scale) is attached at the MT's tip, which freely fluctuates in the medium ($\delta \equiv$ deflection). Both δ and the MT bending profile are exaggerated for illustration purposes. The distance of the MT from both sides of the chamber is at least 20 μm. (*b*) Sequence of three frames showing the attachment of an optically trapped 250-nm fluorescent bead (arrows) to the tip of a grafted MT (frames 1 and 2; a shadowing routine was applied to enhance the contrast). After changing the filters set, only the fluorescence from the bead is detected (frame 3).

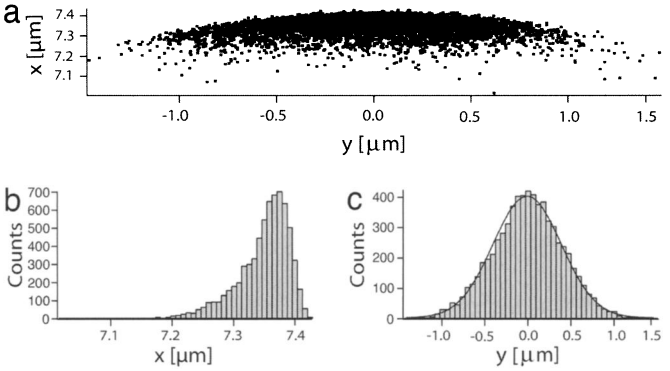

Fig. 2. Probability distributions of the MT tip position. (*a*) Bead's position tracked over 10^4 frames. The bead has a diameter of 250 nm and is attached at the tip of a MT with a contour length of 7.2 μm. (*b*) Reduced distribution function along the *x* axis (see Fig. 1*a*). (*c*) Reduced distribution function along the *y* axis. The experimental points distribution $P(y)$ is fitted by a Gaussian distribution the width of which is given by the transverse length scale $L_\perp = \sqrt{(L^3/3\ell_p)}$.

contour reveal its intrinsic stiffness. Although the persistence length ℓ_p has been measured with great accuracy for actin by means of studying $P(R)$ (22), a detailed study of the mechanics of MTs based on probability distributions is complicated by their high stiffness, requiring an assay with very high spatial resolution. Here, we apply single-particle tracking for measuring the probability distribution function $P(x, y)$ of grafted MTs. From the measured probability distributions we obtain the MTs persistence length and systematically investigate its dependence on the total contour length L over a broad range (from 2.6 to 47.5 μm). Thermal fluctuations, as originally suggested by Einstein, represent the most natural way to "probe the intangible" (23), in our case the mechanics of biological nanometer-sized specimens nondestructively and over extended times. Thermal fluctuations already have been taken into account to model the structural and elastic properties of MT tips as evidenced by cryoelectron microscopy (24).

Results

The experimental situation is depicted in Fig. 1 *a* and *b*. In the assay, we select single grafted MTs with one bead attached proximally to the tip. A MT with two free ends would allow only the measurement of $P(R)$: grafting one end of a MT allows for a direct precise measurement of $P(x, y)$ and of the reduced distribution functions $P(x)$ and $P(y)$, which are more sensitive to the elastic parameters and, in our case, allow a precise measurement of ℓ_p. Because the beads and the MTs emit fluorescence at two different wavelengths, they can be observed independently by simply exchanging the filter set in the microscope. The attached bead acts as a neutral tracer. Fig. 2*a* shows an example of the distribution resulting from the projection of the three-dimensional fluctuations of the MT's tip on the x, y plane. The distribution is obtained by measuring the position of the fluorescent bead attached at the MT's end in at least 10^4 frames. Measuring the tip's deflection by tracking a strongly fluorescent bead allows one to evaluate with great precision the rigidity of very short MTs, whereas measuring fluctuations in shape on short MTs (3–5) might be problematic, given the much smaller amplitude of the fluctuations. The bead's position is automatically tracked frame-by-frame with a custom particle-tracking routine. The coordinates of the bead's centroid can be determined with an accuracy of 1 nm and better under optimal conditions (25). Here, the accuracy was reduced to $\approx$10 nm. A stack containing the fluorescent MTs is recorded separately for the determination of L.

The recorded particle position is used to obtain the probability distribution function $P(x, y)$ of the free end in the x, y plane and the corresponding reduced distribution functions $P(x)$ and $P(y)$ (Fig. 2 *b* and *c*), obtained by integrating $P(x, y)$ over the coordinates y and x, respectively. These can be directly compared with theoretical predictions based on the worm-like chain model, as reported in ref. 26. Given the high persistence length of a MT (ℓ_p/L can be as high as several hundred), the longitudinal distribution function $P(x)$ is peaked toward full stretching, as in Fig. 2*b*, and varies over a typical length scale $L_\parallel = L^2/\ell_p$. A non-Gaussian and asymmetric shape of $P(x)$ is clearly visible in Fig. 2*b*. In contrast, $P(y)$ is a Gaussian the width of which is given by the transverse length scale $L_\perp = \sqrt{(L^3/3\ell_p)}$, as represented in Fig. 2*c* (27, 28). By measuring the contour length L, ℓ_p can be extracted from both $P(x)$ and $P(y)$. The measured $P(x)$ and $P(y)$ correspond to convolution products between the theoretical functions $P_{th}(x)$ and $P_{th}(y)$ predicted by the worm-like chain model (27, 28) and the function that represents the experimental precision in the measurement of the distance between the tip of the filament and the attachment point on the substrate. Because longitudinal and transverse fluctuations scale differently, the convolution has a negligible effect on $P_{th}(y)$, in contrast to $P_{th}(x)$, the shape of which is much more sensitive to small variations of the experimental precision. For this reason, we focused on $P(y)$ for the determination of ℓ_p in this work. The persistence lengths obtained from $P(y)$ for 48 grafted MTs of different contour

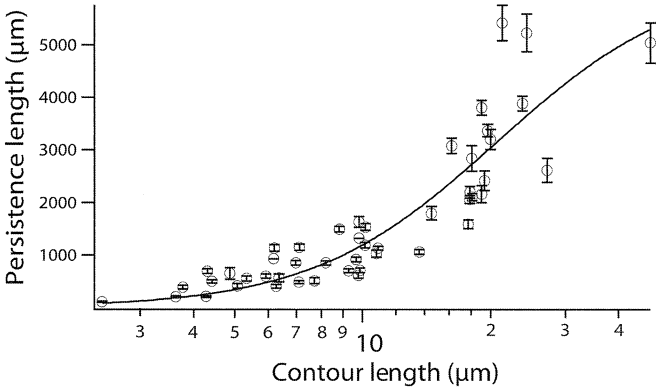

Fig. 3. The persistence length of MTs as a function of their contour lengths. The contour length ranges from 2.6 to 47.5 μm. The fit with Eq. **4** is superimposed on the experimental points.

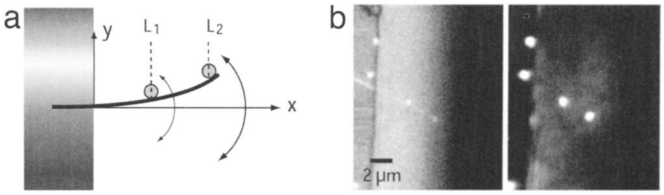

Fig. 4. Consistency check of ℓ_p. (*a*) Thermal fluctuations of two beads attached at the tip (distance L_2) and at a different location (distance L_1) of a grafted MT are measured. (*b*) The real experiment. The MT persistence lengths obtained from beads 1 and 2 on the same MT are compared. For example, the fluctuations of a bead attached at a distance $L_2 = L = 9.2$ μm yield a persistence length of 888 ± 51 μm. The persistence length resulting from thermal fluctuations of the second bead at a distance $L_1 = 4.4$ μm is 862 ± 72 μm. The persistence length of a MT is defined by its total contour length and does not vary continuously along the MT.

lengths are shown in Fig. 3. For a given length L, we have attached beads at different locations along the MT. Fig. 4 shows a typical realization of the experiment: we found that the persistence lengths independently obtained from the fluctuations of the two beads were consistent with ℓ_p being independent on the arc-length position along the contour of the MT.** On the contrary, upon variation of L between 2.6 and 47.5 μm, we observe a systematic increase of ℓ_p from a minimum value of 110 μm to a maximum of 5,035 μm.

As shown in Fig. 3, the values of ℓ_p measured on MTs spread with increasing L. This spreading might be partially due to differences in the structures of single MTs. In fact, in MTs polymerized *in vitro* the number of PFs may vary from one MT to another and even along a given MT, and several lattice types are possible (29). The probability of defects in the MT lattice may also increase with the contour length. Because there is also evidence that the stiffness of MTs can vary with the polymerization velocity (4), we carefully monitored the MT polymerization temperature. The diameter of the bead is much larger than the MT's diameter; thus, the viscous drag acting on the bead is large and will influence the motion of the MT. However, at the time scale of video microscopy-based single-particle tracking (in our case 16 frames per s, corresponding to a time resolution of ≈60 ms) the influence of the bead size is negligible and the fluctuations of the bead reflect accurately the thermal motion of the bare MT's tip.†† The tip of the MT in our assay is at a distance of tens of micrometers from the coverslips; hence, we can neglect hydrodynamic coupling and direct nonspecific interaction with the surface. A potential experimental source of error might be a loose binding of the bead to the MT, which could lead to an underestimation of ℓ_p. This issue has been tested by pulling the bead with optical tweezers at high laser power, ensuring that it attaches firmly to the MT and does not roll or twist on it. In addition, by strongly bending the MT with optical tweezers, we ensured that the segment of the MT anchored to the substrate does not change its orientation during thermal fluctuations, a further possible source of uncertainty in the measurement of ℓ_p. Theoretical calculations show also that the fluctuations of the angle of torsion along the whole MT are below 7° and can be safely neglected.

Linear Elasticity Theory for Composite Structures

It is known that linear elasticity theory works well to model the mechanical properties of nanometer-sized materials, like biofilaments and carbon nanotubes (31, 32). As shown in ref. 24, the various shapes observed at the MT's tip and its mechanical properties can be explained by applying an elastic sheet model in the framework of linear elasticity theory. Because a MT is a tubular assembly of discrete PFs assembled in parallel, its mechanical response can be understood by analogy with anisotropic *fiber reinforced materials* (33) rather than by a direct application of the theory of elasticity for homogeneous structures (34, 35).

The description of the stress–strain relationship in a generally anisotropic structure requires the introduction of a 6 × 6 stiffness matrix containing the elastic moduli along the different orientations and the couplings between different strains. In an isotropic structure, off-diagonal elements (coupling terms) become zero, and the independent elastic parameters reduce to 3: the Young modulus E, the shear modulus G, and the Poisson ratio v. Given their cylindrical symmetry and the PF structure, MTs are transversely isotropic, meaning that they are anisotropic along the longitudinal direction, whereas their cross section has an isotropic response to stresses (Fig. 5). For transversely isotropic materials, the tensile/compressive stress–strain relationship is expressed by (33)

$$\begin{pmatrix}\sigma_x\\ \sigma_y\\ \sigma_z\end{pmatrix} = \begin{bmatrix} E_1 & -E_2/\nu_{21} & -E_2/\nu_{21} \\ -E_1/\nu_{12} & E_2 & -E_2/\nu_{23} \\ -E_1/\nu_{12} & -E_2/\nu_{23} & E_2 \end{bmatrix} \begin{pmatrix}\varepsilon_x\\ \varepsilon_y\\ \varepsilon_z\end{pmatrix}, \quad [1]$$

where σ_x, σ_y, and σ_z are the stresses along the x, y, and z axes and ε_x, ε_y, and ε_z are the corresponding strains; E_1 and E_2 are the longitudinal and transverse Young moduli, respectively, and ν_{12}, ν_{21}, and ν_{23} are the Poisson ratios.‡‡ The shear stress–strain relationships are described by the following matrix:

**This experiment is also relevant to confirming the reliability of our approach: Thermal fluctuations of the MT's tip are basically related to the first bending mode of the MT, which is very sensitive to flows of the liquid in the sample (3–5) and induces a large experimental error. This problem is less critical when measuring equilibrium fluctuations, as in our case, but still requires a very good control over the experimental conditions. By measuring the fluctuations of two beads at two different positions of the same MT, we obtain two independent and consistent measurements of ℓ_p, thus confirming the reliability of our assay.

††According to ref. 22, the relaxation time for the first bending mode of a semiflexible polymer is $\tau = (\zeta/\ell_p k_B T)(L/A)^4$, where $\zeta = 2.47 \times 10^{-3}$ Pa s is an effective friction coefficient and $A = 1.875$ for a polymer with one clamped and one free end. We find that $\tau = 76.6$ ms for a MT of 10 μm: This estimate has been compared with relaxation times extracted from our data by analyzing the power spectra of the thermal fluctuations and, as an independent consistency check, by calculating the histograms of the tip displacements at varying delay times. Interestingly, we found that the experimental relaxation times were systematically longer than expected from theoretical estimates. Unexpectedly long relaxation time for MTs were already reported in the literature, and they may be interpreted as the result of an internal friction effect within the MT (4). As far as our measure of $P(y)$ is concerned, the set charge-coupled device camera integration time is short enough compared with the relaxation time of the MT thermal fluctuations, and the width of the experimental $P(y)$ is not artificially narrowed. However, the total observation time largely exceeds the MT relaxation time in the range of contour lengths examined, so that the width of $P(y)$ is always measured at its equilibrium value (see ref. 30).

‡‡Symmetry considerations impose that $E_2/\nu_{21} = E_1/\nu_{12}$, so that there are four independent elastic parameters.

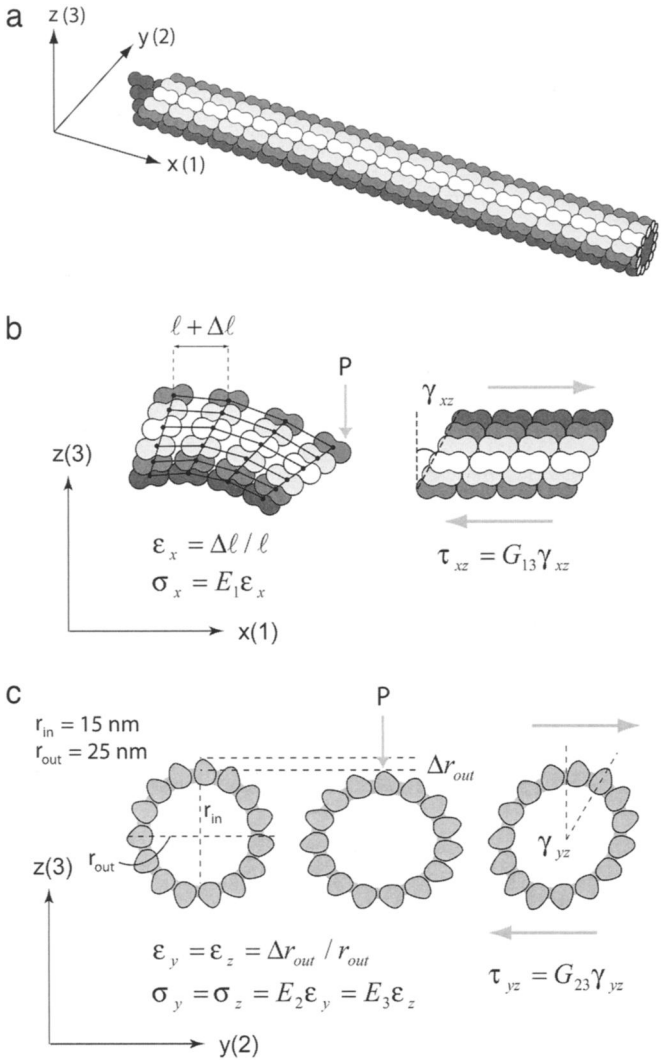

Fig. 5. Mechanical anisotropy of a MT. (*a*) *x*, *y*, and *z*, geometrical axes; 1, 2, and 3, material axes of the MT. (*b*) Bending generates a tensile/compressive stress $\sigma_x = E_1\varepsilon_x$ and a shear stress $\tau_{xz} = G_{13}\gamma_{xz}$ between adjacent PFs (E_1 and G_{13} are longitudinal Young's and shear modulus, respectively; *P* is the load, ε_x is the tensile strain along *x*, and γ_{xz} is the longitudinal shear strain). Given the anisotropy in the tubulin interaction across and along PFs, E_1 and G_{13} may differ by several orders of magnitude. (*c*) Similarly to fiber-reinforced materials, MTs are transversely isotropic, implying that on the plane of the cross section $E_2 = E_3$ and that the Poisson's relationship between the Young's modulus and the transverse shear modulus G_{23} still holds.

$$\begin{pmatrix}\tau_x\\ \tau_y\\ \tau_z\end{pmatrix} = \begin{bmatrix}G_{13} & 0 & 0\\ 0 & G_{13} & 0\\ 0 & 0 & G_{23}\end{bmatrix}\begin{pmatrix}\gamma_{xy}\\ \gamma_{xz}\\ \gamma_{yz}\end{pmatrix}. \qquad [2]$$

Here, τ_i is the shear stress along the *i* direction, and γ_{ij} represents the strain angle in the *ij* plane. In transversely isotropic materials there is no coupling between transverse (G_{23}) and longitudinal (G_{13}) shear moduli. Conversely, the transverse shear and Young moduli are linked by the relationship $G_{23} = E_2/2(1 + \nu_{23})$, given the transverse isotropy.[§§]

Discussion

In the following discussion, we will model MTs as transversely isotropic hollow cylindrical beams and assume that the small fluctuations in the tip's position can be interpreted as deflections due to thermal forces. Given the boundary conditions and the geometry of the system, only the elastic moduli E_1 and G_{13} are involved in bending on the *x*, *y* plane. By assuming the deflection as due to a point load *P* applied at the free end of the grafted filament, the total deflection of the MT (δ) is the sum of both bending (δ_B) and shear deformations (δ_S) (10, 33):

$$\delta = \delta_B + \delta_S = \frac{PL^3}{\alpha E_1 I_2} + \frac{PL}{G_{13}kA} = \frac{PL^3}{\alpha \ell_p k_B T}, \qquad [3]$$

where *P* is the lateral load at the MT's tip, $I_2 = 1/4\pi(R_e^4 - R_i^4)$ is the second moment of the tube's cross-sectional area *A*, and *k* is a geometrical correction factor the value of which is 0.72 for a hollow cylindrical beam (36) and $\alpha = 3$ for a grafted beam. The last equality, with k_BT the thermal energy, represents the linear response of a polymer with persistence length ℓ_p in the same loading configuration and with the same boundary conditions (37). Through the relationship $E_1I_2 = \ell_p^\infty k_BT$, Eq. **3** can be used to obtain the length dependence of ℓ_p:

$$\ell_p = \ell_p^\infty\left(1 + \frac{3E_1I_2}{G_{13}kAL^2}\right)^{-1}, \qquad [4]$$

where ℓ_p^∞ is the persistence length for "long" MTs ($L \gg \sqrt{3E_1I_2/G_{13}kA} \approx 21\ \mu$m). This relationship does not depend on the nature of the applied force; hence, fluctuations due to thermal forces are perfectly suitable for its direct test. Eq. **4** provides a good fit to the experimental points, giving a value of $\ell_p^\infty = 6.3 \pm 0.8$ mm in agreement with previous measurements on taxol-stabilized MTs (4). This value corresponds to $E_1 = 1.51 \pm 0.19$ GPa and a ratio of $\delta_S/\delta_B = (21/L)^2$ when *L* is expressed in micrometers, corresponding to an extremely large ratio $E_1/G_{13} \sim 10^6$. This result is surprising and must be interpreted carefully. First, it is important to remark that E_1 and G_{13} are not linked in this case by the Poisson relationship $G = E/2(1 + \nu)$, because of the mechanical anisotropy on the plane *xz*(*xy*). Hence, a large E_1/G_{13} ratio does not imply an exceedingly high ν_{13}, which would lead to a diagonal collapse (complete flattening) of the cross section upon bending. Second, at microscopic level a very small shear modulus G_{13} implies a high compliancy of the lateral inter-PF bonds.

From electron microscopy studies, it is known that the compliancy of inter-PF bonds allows one to accommodate a broad range of structures of the MT lattice, which can differ in PFs and helix-start numbers (19, 38–40). Variability within a range of ± 0.2 nm in the relative position of tubulin dimers on adjacent PFs was also observed in these studies and interpreted as the result of thermally driven deformations of the lateral contacts between PFs (19, 38). Electron crystallography maps obtained at 8- and 20-Å resolution give insight about the molecular origin of longitudinal and lateral interactions in MTs (41, 42). One key structural element in determining lateral interactions between dimers is a long loop (the S7–H9 loop, also called "M-loop"; Fig. 6*c*) that protrudes from the PF side, interacting with the loop H1–S2 and the α-helix H3 on the surface of the neighboring PF (41, 42). Such interaction involves an important electrostatic contribution, at variance with the $\alpha\beta$–$\alpha\beta$ tubulin bonds along the PF, which are linked by prevalently hydrophobic and polar interactions on a very large interface ($\approx$3,000 Å^2) and with extremely high complementarity in shape, thus suggesting that short-range Van der Waals forces are important in intra-PF contacts between tubulins (41, 42). It is known that head–tail intra-PF contacts between tubulin dimers are stronger than lateral inter-PF contacts. Sept *et al.* (18) have calculated that longitudinal bonds along the PF are 7 kcal/mol stronger than lateral ones. Estimating the elastic constant of a single longitudinal bond from the potential profile calculated by Sept *et al.*

[§§]The total number of independent elastic parameters is thus 5.

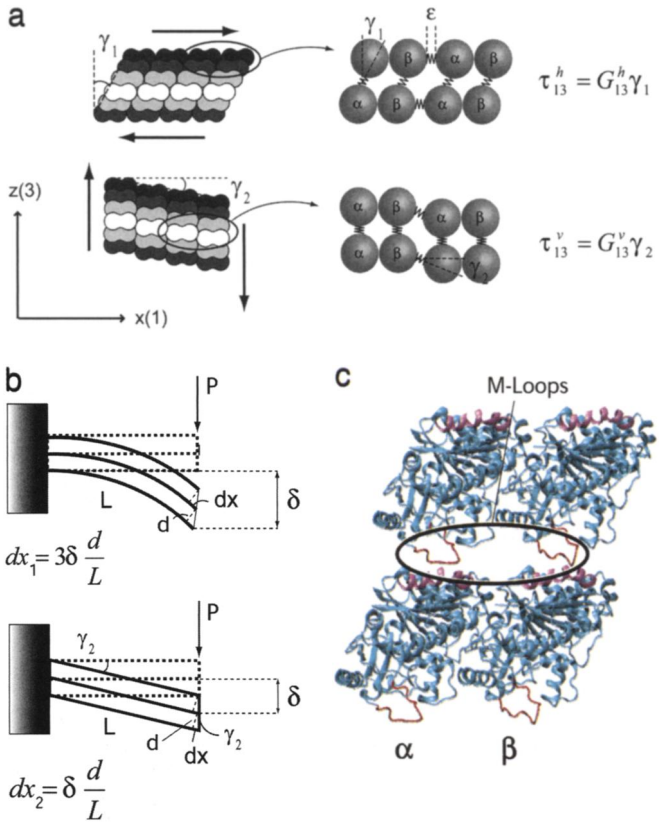

Fig. 6. Deformations due to shear stress in a MT. (*a Upper*) Shear stress originated by distortion of the inter-PF bonds. (*a Lower*) Shear stress due to distortion of the intra-PF bonds between tubulin dimers. (*b*) A simplified model of a two-dimensional grafted MT composed by two PFs is used to obtain an estimate of the shift (*dx*) between two adjacent PFs due to shear stress. The visualizations in *b* show how the toy MT would deform in the (impossible) case of a shear force being constant along the length (τ is *x*-independent) and the bending moment being *zero* everywhere (this idealized situation is called "pure shear"). (*b Upper*) Shift related to the deformation of inter-PF bonds by bending (refer to *a Upper*). No lateral links are assumed, so that the two PFs can freely slide past each other. Moreover, the bending profile of the MT is assumed to be circular. (*b Lower*) Shift related to the deformation of intra-PF bonds. Taking $L = 10\ \mu$m, $d = 4$ nm, $\delta = 0.5\ \mu$m, $dx_1 = 0.6$ nm, and $dx_2 = 0.2$ nm, respectively. (*c*) Image created with VMD (47). The PFs are laterally linked together by the flexible M-loops (orange) and the α-helix H3 (magenta).

results in $k_{\text{long}} = 4$ N/m (43), which is 40 times larger than the elastic constant measured in a transverse compression by an AFM tip, $k_{\text{trans}} = 0.1$ N/m (7). Thus, a large amount of experimental data, including the assembly/disassembly dynamics of MTs, electron crystallography maps (41, 42), cryoelectron microscopy (19, 38, 44), and small-angle x-ray diffraction (21, 45), suggest a pronounced mechanical anisotropy of MTs.

Microscopically, the longitudinal elastic modulus E_1 is expected to arise from the strong $\alpha\beta$–$\alpha\beta$ tubulin bonds along single PFs, whereas the M-loop might be the prevalent contribution to the longitudinal shear modulus G_{13}. The energy barrier adjacent PFs must overcome to produce the tiny relative displacement observed by electron microscopy is likely very small [on the order of thermal fluctuations (19)], at least for small strains within 0.2 nm (19, 38, 44). Therefore, MTs could easily absorb shear stresses associated with bending by slightly shifting the relative position of neighboring PFs. Indeed, our measurement of a very large E_1/G_{13} ratio confirms such a hypothesis. As shown in Fig. 6, we estimate the amount of PF shear strain produced by the observed MT deflection to be on the subnanometer scale and hence consistent with the measurements of PF relative displacement provided by cryoelectron microscopy (19, 38, 44). For forces larger than the thermal force, the compliance of the lateral connection between PFs might be eventually exceeded, leading to deformation of tubulin subunits. Higher forces can be obtained, for instance, by further increasing the osmotic pressure in the medium (45). Tubulin subunits have a high stiffness, typical of proteins, of ≈2 GPa (46). Deformation of the stiff tubulin dimers might be the explanation of the postbuckling elastic response measured in ref. 45. The shear modulus G_{13} may be considered as the result of two possible contributions: a vertical shear modulus (G_{13}^{v}) arising from stretching of intra-PF tubulin, and a horizontal shear modulus (G_{13}^{h}), determined by lateral bonds between PFs (Fig. 6). The above-mentioned structural considerations imply that $G_{13}^{\text{h}} \ll G_{13}^{\text{v}}$. Consequently, the shear deflection is given by

$$\delta_{\text{S}} = \frac{PL}{kA}\left(\frac{1}{G_{13}^{h}} + \frac{1}{G_{13}^{v}}\right) \qquad [5]$$

and, in the case of a thermally fluctuating MT, would be largely dominated by the horizontal shear modulus, determined by the compliance of inter-PF bonds. In case a cross-linker like glutaraldehyde is present to stabilize MTs, the relative displacement between PFs would be hindered and the magnitude of G_{13}^{h} and G_{13}^{v} would be comparable, thus implying a higher overall value of G_{13} and a lower E_1/G_{13} ratio. This stabilization partly explains the difference between our results and the E/G ratio previously reported in AFM experiments on glutaraldehyde-stabilized MTs (9, 10). In contrast, to stabilize MTs we used the drug taxol, which inserts in the MT lattice and may relieve the MT internal tension inducing a further decrease of the shear modulus (11). In addition, AFM experiments (7, 9, 10) are likely to probe the structure of MTs by involving the transversal modulus G_{23}, whereas the main contribution to shear stress in our thermal bending experiments is given by G_{13}. Consequently, the E/G ratio measured in AFM experiments is likely different from the E_1/G_{13} ratio measured in this work.

Conclusions

We have developed an assay based on single-particle tracking to measure the reduced distribution functions $P(x)$ and $P(y)$ for the tip's position of grafted MTs with high spatial resolution. Through our fluctuation analysis, we have found a systematic and strong increase of MT persistence length with the total contour length L. For short MTs ($L = 2$–$3\ \mu$m), we observe an ℓ_{p} on the order of a few hundred micrometers, at least one order of magnitude smaller than for long ones ($L \geq 30$–$40\ \mu$m). This property can be explained by the anisotropic structure of MTs and described by linear elasticity theory. Our results together with those in refs. 9, 10, and 21 suggest that the inter-PF bonds are highly compliant (at least for small strains), leading to a very low longitudinal shear modulus G_{13} in MTs. The dependence of ℓ_{p} on L in MTs might also contribute to explaining the broad range of measured MT persistence lengths found in the literature for taxol-stabilized and bare MTs (0.5–8 mm) (3, 4, 11). Noticeably, the maximum variability of ℓ_{p} occurs at contour lengths close to the typical length scale of a cell ($L \approx 12\ \mu$m). It is interesting to speculate about the biological significance of this property. MTs are able to accomplish various tasks in differently sized cells and during different stages of a cell's life cycle. On one hand, the flexibility of a MT allows it to search space laterally for binding partners or to bend and continue growing in a modified direction when encountering obstacles, for example when growing MTs hit the side of a small fission yeast cell. On the other hand, sufficient rigidity is important in situations in which MTs need to resist pushing forces such as in large vertebrate cells during anaphase of mitosis, when the spindle elongates. The length dependence of MT rigidity might have allowed cells

during evolution to use MTs in an optimal way both for lateral searching and for exerting pushing forces in different contexts and especially on different length scales.

Materials and Methods

Biotinylated tetramethylrhodamine-labeled MTs (25 μM pig brain tubulin dimers of which 10% was labeled and 10% was biotinylated) were polymerized for 20 min at 37°C with 2 mM GTP in BRB80 buffer (80 mM Pipes, pH 6.8/2 mM $MgCl_2$/1 mM EGTA). After polymerization, MTs were centrifuged at 215,000 $\times$ g and washed once with BRB80. Pellets were resuspended in 20 μM paclitaxel (Sigma-Aldrich) solved in BRB80 buffer.

A gold grid for transmission electron microscopy with linear mesh (Agar) was glued onto a round glass coverslip (170 μm thick and 15 mm in diameter; Menzel-Gläser, Braunschweig, Germany) by a tiny amount of a fluid silicon rubber (Elastosil E43; Wacker Chemie) deposited carefully onto the grid's rim. After drying of the adhesive, the grid surface was treated with a basic/oxidizing cleaning solution ($H_2O_2/NH_3/H_2O$, 1:1:5 volumes) for 1 h. The mounted grid was then rinsed with deionized water and ethanol and incubated overnight with a 5 mM solution of mercaptoundecanoic acid (Sigma-Aldrich) to obtain an ordered self-assembled monolayer with the reactive carboxylic groups exposed toward the outside on the gold surface. After overnight incubation the grid was washed with ethanol and dried with a nitrogen flow. A flow chamber was then realized by mounting the coverslip with the grid onto a rectangular one (30 $\times$ 22 mm) with double-sided adhesive tape as a spacer. The distance between the grid and the bottom coverslip was 30–40 μm, and the total volume of the flow cell was $\approx$20 μl. The exposed carboxylic groups were activated by flowing into the chamber 20 μl of an aqueous solution of 100 mM *N*-hydroxysuccinimide and 100 mM EDC (both from Sigma-Aldrich).

The MT suspension was diluted 1:100 (vol/vol) in 20 μM paclitaxel/BRB80. About 20 μl of the MTs' suspension was made to flow into the chamber and incubated for 1/2 h. Subsequently, $\approx$20 μl of an oxygen scavenger solution (hemoglobin diluted 1:22 from a saturated solution, 0.5 mg/ml glucose oxidase/0.14 mg/ml catalase/46 mM glucose) in 20 μM BRB80/paclitaxel, containing a diluted suspension of beads, was exchanged in the flow chamber. The beads were neutravidin-coated and yellow-green fluorescent with a diameter of 250 or 500 nm (F8811 and F8813; Molecular Probes; excitation 505 nm, emission 515 nm). The chamber was finally sealed with a small quantity of silicon grease at both ends to avoid evaporation of the medium.

The single-particle tracking set-up was based on a conventional epifluorescence microscope (Axiovert; Zeiss) (25). The MTs and the beads, fluorescing, respectively, at 585 and 515 nm, were imaged by using a peltier-cooled sensitive camera (Sensicam; PCO). MTs with a single bead attached at the tip were selected for the measurement. Alternatively, optical tweezers were used for attaching the bead. A stack of 10^4 frames of the bead's thermal fluctuations were recorded for each MT, at a rate of 16 frames per s, setting an integration time of 25–50 ms. Each stack was processed by tracking automatically the bead's position in each frame by a custom particle-tracking routine implemented with the data analysis software IGOR PRO (WaveMetrics) (25).

We acknowledge helpful discussions with J. Howard and C. F. Schmidt. We thank A. Rohrbach, E. H. K. Stelzer, and J. Swoger for substantial support and many interesting discussions. G.L. was supported by European Commission Contracts HPMF-CT-2001-01432 and MERG-CT-2004-513598. F.P. was supported by German Research Foundation Grant FL351/2-1.

1. Nédélec, F., Surrey, T. & Karsenti, E. (2003) *Curr. Opin. Cell Biol.* **15,** 118–124.
2. Bray, D. (2001) in *Cell Movements: From Molecules to Motility* (Garland, New York), p. 192.
3. Gittes, F., Mickey, E. & Nettleton, J. (1993) *J. Cell Biol.* **120,** 923–934.
4. Janson, M. E. & Dogterom, M. (2004) *Biophys. J.* **87,** 2723–2736.
5. Mickey, B. & Howard, J. (1995) *J. Cell Biol.* **130,** 909–917.
6. Venier, P., Maggs, A. C., Carlier, M. F. & Pantaloni, D. (1994) *J. Biol. Chem.* **269,** 13353–13360.
7. de Pablo, P. J., Schaap, I. A. T., MacKintosh, C. & Schmidt, C. F. (2003) *Phys. Rev. Lett.* **91,** 098101.
8. Schaap, I. A. T., de Pablo, P. J. & Schmidt, C. F. (2004) *Eur. Biophys. J.* **33,** 462–467.
9. Kasas, S., Kis, A., Riederer, M., Forrò, L., Dietler, G. & Catsicas, S. (2004) *ChemPhysChem* **5,** 252–257.
10. Kis, A., Kasas, S., Babič, B., Kulik, A. J., Benoît, W., Briggs, G. A. D., Schönenberger, C., Catsicas, S. & Forrò, L. (2002) *Phys. Rev. Lett.* **89,** 248101.
11. Felgner, H., Frank, R. & Schliwa, M. (1996) *J. Cell Sci.* **109,** 509–516.
12. Felgner, H., Frank, R., Biernat, J., Mandelkow, E., Ludin, B., Matus, A. & Schliwa, M. (1997) *J. Cell Biol.* **138,** 1067–1075.
13. Kurachi, M., Hoshi, M. & Tashiro, H. (1995) *Cell Motil. Cytoskeleton* **30,** 221–228.
14. Kratky, O. & Porod, G. (1949) *Recl. Trav. Chim. Pays Bas* **68,** 1106–1123.
15. Saito, N., Takahashi, K. & Yunoki, Y. (1967) *J. Phys. Soc. Jpn.* **22,** 219–226.
16. Wilhelm, J. & Frey, E. (1996) *Phys. Rev. Lett.* **77,** 2581–2584.
17. Van Buren, V., Odde, D. J. & Cassimeris, L. (2002) *Proc. Natl. Acad. Sci. USA* **99,** 6035–6040.
18. Sept, D., Baker, N. A. & McCammon, J. A. (2003) *Protein Sci.* **12,** 2257–2261.
19. Hunyadi, V., Chrétien, D. & Jànosi, I. M. (2005) *J. Mol. Biol.* **348,** 927–938.
20. Kasas, S., Cibert, C., Kis, A., Rios, P. D. L., Riederer, B., Forrò, L., Dietler, G. & Catsicas, S. (2004) *Biol. Cell* **96,** 697–700.
21. Needleman, D. J., Ojeda-Lopez, M. A., Raviv, U., Ewert, K., Jones, J. B., Miller, H. P., Wilson, L. & Safinya, C. R. (2004) *Phys. Rev. Lett.* **93,** 198104.
22. LeGoff, L., Hallatschek, O., Frey, E. & Amblard, F. (2002) *Phys. Rev. Lett.* **89,** 258101.
23. Frey, E. & Kroy, K. (2005) *Ann. Phys. (Leipzig)* **14,** 20–50.
24. Janosi, I. M., Chretien, D. & Flyvbjerg, H. (1998) *Eur. Biophys. J.* **27,** 501–513.
25. Speidel, M., Jonáš, A. & Florin, E.-L. (2003) *Opt. Lett.* **28,** 69–71.
26. Lattanzi, G., Munk, T. & Frey, E. (2004) *Phys. Rev. E* **69,** 021801.
27. Benetatos, P. & Frey, E. (2003) *Phys. Rev. E* **67,** 051108.
28. Gholami, A., Wilhelm, J. & Frey, E. (2006) *Phys. Rev. E*, cond-mat/0603101.
29. Chrétien, D., Metoz, F., Verde, F., Karsenti, E. & Wade, R. H. (1992) *J. Cell Biol.* **117,** 1031–1040.
30. Caspi, A., Elbaum, M., Granek, R., Lachish, A. & Zbaida, D. (1998) *Phys. Rev. Lett.* **80,** 1106–1109.
31. Wong, E. W., Sheehan, P. E. & Lieber, C. M. (1997) *Science* **277,** 1971–1975.
32. Cohen, A. E. & Mahadevan, L. (2003) *Proc. Natl. Acad. Sci. USA* **100,** 12141–12146.
33. Kollár, L. P. & Springer, G. S. (2003) *Mechanics of Composite Structures* (Cambridge Univ. Press, Cambridge, U.K.), pp. 19–20.
34. Timoshenko, S. & Goodier, J. N. (1970) *Theory of Elasticity* (McGraw–Hill, New York).
35. Landau, L. D. & Lifšits, E. M. (1959) *Course of Theoretical Physics* (Pergamon, London), Vol. 7.
36. Kis, A. (2003) Ph.D. thesis (Ecole Polytechnique Fédérale de Lausanne, Lausanne, Switzerland), http://library.epfl.ch/theses/?nr=2876.
37. Kroy, K. & Frey, E. (1996) *Phys. Rev. Lett.* **77,** 306–309.
38. Chrétien, D. & Fuller, S. D. (2000) *J. Mol. Biol.* **298,** 663–676.
39. Chrétien, D. & Wade, R. H. (1991) *Biol. Cell* **71,** 161–174.
40. Keskin, O., Durell, S. R., Bahar, I., Jernigan, R. L. & Covell, D. G. (2002) *Biophys. J.* **83,** 663–680.
41. Nogales, E., Whittaker, M., Milligan, R. A. & Downing, K. H. (1999) *Cell* **96,** 79–88.
42. Li, H., DeRosier, D. J., Nicholson, W. V., Nogales, E. & Downing, K. H. (2002) *Structure (London)* **10,** 1317–1328.
43. Tuszýnski, J. A., Luchko, T., Portet, S. & Dixon, J. M. (2005) *Eur. Phys. J.* **17,** 29–35.
44. Chrétien, D., Flyvbjerg, H. & Fuller, S. D. (1998) *Eur. Biophys. J.* **27,** 490–500.
45. Needleman, D. J., Ojeda-Lopez, M. A., Raviv, U., Ewert, K., Miller, H. P., Wilson, L. & Safinya, C. R. (2005) *Biophys. J.* **89,** 3410–3423.
46. Howard, J. (2001) *Mechanics of Motor Proteins and the Cytoskeleton* (Sinauer, Sunderland, MA), pp. 148–149.
47. Humphrey, W., Dalke, A. & Schulten, K. (1996) *J. Mol. Graphics* **14,** 33–38.